Oxygen defect formation and migration in $Sr_2FeO_{4-\delta}$: Insights from first principles DFT calculations with the PBE + U functional

Yuri A. Mastrikov,[1,2,*] Denis Gryaznov,[1,†] Andrew Chesnokov,[1] Guntars Zvejnieks,[1] Maksim Sokolov,[1,3] Maija M. Kuklja,[2] Rotraut Merkle,[4] and Eugene A. Kotomin[1,4]

[1]*Institute of Solid State Physics, University of Latvia, 8 Ķengaraga Street, Rīga, LV-1063, Latvia*
[2]*University of Maryland College Park, College Park, Maryland 20742, USA*
[3]*University of Duisburg-Essen, Universitätsstraße 2, D-45141 Essen, Germany*
[4]*Max Planck Institute for Solid State Research, Heisenbergstraße 1, D-70569, Stuttgart, Germany*

(Received 23 September 2024; accepted 23 May 2025; published 30 October 2025)

$Sr_2FeO_{4-\delta}$ is a first-order Ruddlesden-Popper perovsike-type material, prospective as a positrode (O-electrode) material for solid oxide and protonic ceramic electrochemical cells. By means of DFT + U_{eff}, oxygen vacancies ($V_O^{\bullet\bullet}$) and interstitials (O_i'') have been modelled in a broad oxygen stoichiometry range of $\delta = 0.125$ to 0.5. For each δ value, all symmetry inequivalent configurations were identified, yielding the $V_O^{\bullet\bullet}$ formation energy in the range of 2.0–2.4 eV, almost independent of δ (unlike for simple perovskites). We assign the individual Fe charge states in $Sr_2FeO_{4-\delta}$ ("*oxidation state map*") based on magnetic moment and average Fe-O distance. Interestingly, $V_O^{\bullet\bullet}$ and Fe^{3+} energetically prefer not to be nearest neighbors. Regarding oxygen interstitial species, a Sr-O_2^{2-}-Fe defect is the most stable form. Oxygen interstitial transport mechanism occurs predominantly within the SrO layer with the intermediate formation of a single oxide O_i^{2-} and an average barrier of 0.5 eV. Oxygen vacancy migration is preferred along a zig-zag path within the FeO_2 layer with an effective barrier of 0.6 eV. The comprehensive analysis of $Sr_2FeO_{4-\delta}$—serving as prototype also for higher Ruddlesden-Popper phases—including oxidation state map and oxygen defect migration, paves the way for coming investigations of the protonated materials.

DOI: 10.1103/v8m7-prgq

I. INTRODUCTION

Air electrodes (positrodes) for solid oxide and protonic ceramic electrochemical cells (SOC's and PCC's) have to be chosen on the basis of materials functionality and should mainly be based on easily available/low-cost elements. Several important material properties need to be taken into account, as summarized in recent reviews [1–4]. An appropriate combination of electronic, oxide ion, and proton conductivities is decisive, motivating the search for triple-conducting air electrode materials for PCCs with fast oxygen reduction surface kinetics, good chemical stability, and thermal (chemical) expansion properties that can be matched to the respective electrolyte materials. Most triple-conducting oxides investigated so far stem from the family of perovskite or closely related structures (double perovskites, Ruddlesden-Popper [5] (RP) phases).

The layered RP phases $A_{n+1}B_nO_{3n+1}$ attract attention due to their ability to accommodate oxygen vacancies ($V_O^{\bullet\bullet}$) and oxygen interstitials (O_i'') on the oxygen sublattice (using Kröger-Vink notation [6]). The higher ratio of basic A-site cations to less basic B-site cations compared to ABO_3 perovskites (for example, $BaFeO_3$-based materials [7,8]) is expected to be beneficial for proton incorporation. Mixed conducting RP phases, typically first up to the third order (n = 1–3), cover a large range of compositions, with alkali-earth and/or rare-earth cations on the A site and mainly Fe, Co, Ni, Cu on the B site. For SOC applications, $Ln_{n+1}Ni_nO_{3n+1}$ without alkali-earth cations have received large interest (see, e.g., Refs. [9–14]). Proton conduction has been discussed in $La_2NiO_{4+\delta}$ [15] and $Pr_2NiO_{4+\delta}$-based materials [16,17]. Cobalt-based RP phases such as $(La, Sr)_2CoO_{4\pm\delta}$, as well as composites with the respective $(La, Sr)CoO_{3-\delta}$ perovskite were mainly studied related to SOCs, e.g., Refs. [18–20]. Iron-based RP phases received increasing interest in the context of PCCs, e.g., $Sr_3Fe_2O_{7-\delta}$ and $Eu_2SrFe_2O_{7-\delta}$ [21–24]. Interestingly, at room temperature to 100 °C, some RP phases even show incorporation of molecular water into the rocksalt-structured AO layers [25,26]. Sr_2FeO_4 has also been studied for its complex magnetic behavour at low temperatures [27].

While both material families become triple conductors under appropriate conditions, it is important to note also characteristic differences between $(La, Sr)FeO_{3-\delta}$ perovskites and the $(La, Sr)_2FeO_{4\pm\delta}$ and $(La, Sr)_3Fe_2O_{7\pm\delta}$ RP phases. The presence of rocksalt-structured (La,Sr)O layers between perovskite blocks not only allows for comparably easy formation of oxygen interstitials, but may also change the character of the electronic structure. For zero or small oxygen deficiency, $SrFeO_{3-\delta}$ exhibits metallic-type electronic conductivity and

*Contact author: yuri.mastrikov@cfi.lu.lv
†Contact author: gryaznov@cfi.lu.lv

absence of Jahn-Teller (JT) distortions (despite formally containing Fe^{4+}, a high-spin $3d^4$ cation) [28]. In contrast, the strontium ferrate RP phases exhibit polaron hopping of electron holes (cf. Refs. [29,30] and results for $Sr_2FeO_{4-\delta}$ in the present paper), indicating a much decreased degree of electronic delocalization. This difference merits a more detailed investigation, in particular as it may affect the propensity for proton uptake as observed in $BaFeO_3$ [8].

While the synthesis of $Sr_2FeO_{4-\delta}$ requires a treatment with high oxygen pressure [31], the second-order RP phase $Sr_3Fe_2O_{7-\delta}$ can be prepared under normal atmosphere, making it the preferred composition for actual electrode materials. However, for the present first principles investigation at the DFT + U_{eff} level, we choose the first-order RP phase $Sr_2FeO_{4-\delta}$, which most strongly demonstrates the differences of RP phases compared to the respective simple perovskite with respect to the *A*:*B* cation ratio as well as electronic structure. We use the methodology of detailed investigations at realistic point defect concentrations [8,32] to closely approach the experimental conditions in which the oxygen nonstoichiometry δ varies as a function of temperature and oxygen partial pressure (e.g., Refs. [27,33,34]). We study both $V_O^{\bullet\bullet}$ and O_i'' to cover a large range of defect concentrations (and correspondingly effective Fe oxidation states ranging from 4+ to 3+, according to the electroneutrality condition), and fully explore the configuration space for the case of multiple $V_O^{\bullet\bullet}$ in the model supercell. We provide a detailed insight into the intricate electronic structure and identify several possible configurations of Fe^{3+} polarons, which is expected to affect the protonation propensity. We also discuss a complete set of $V_O^{\bullet\bullet}$ and O_i'' migration barriers. It is important to explore the full set of defects and their barriers to extend our understanding which parameters affect the barrier heights (geometrical aspects but also persistence or breaking of bonds), and also because the overall conductivity depends on barrier height as well as defect concentration (i.e. even a defect with higher initial energy may significantly contribute when its barrier is substantially lower). Thus, the present work clearly proceeds beyond previous publications [35]. We address the delicate interplay of geometric and electronic structure to achieve a comprehensive understanding of $Sr_2FeO_{4-\delta}$, which is located in a complex transition zone between materials with rather localized electronic structure (such as Ba-rich perovskites and perovskite-related materials with large lattice parameters and correspondingly decreased Fe-O orbital overlap), and perovskites with quite delocalized electronic structure (such as $SrFeO_3$). Such an analysis is also important for further investigations of respective protonated materials, because the propensity of oxygen ions for protonation depends sensitively on the character of the O electronic states.

II. METHOD AND MODEL

A. Computational parameters, crystal structure, and $V_O^{\bullet\bullet}$ formation energy

For modelling the system under study, we applied the DFT + U_{eff} method (hereafter, DFT+*U*) within the simplified Dudarev form [36] using the PBE functional as implemented in Vienna *ab initio* simulation package (VASP) 6.1 [37]. It has been shown for (Ba, Sr)$FeO_{3-\delta}$ [8,38] and (Pr, Sr)$_2FeO_{4-\delta}$ [35] that the chosen value of $U_{\text{eff}} = 4.0$ eV is sufficiently accurate to describe the key parameters of the material: lattice constant and magnetic moments. The transitions between localized and more delocalized states are relevant in $Sr_2FeO_{4-\delta}$ as well. The degree of localization is expected to increase with higher values of δ upon transition from the average oxidation state of Fe^{4+} ($\delta = 0$) to Fe^{3+}($\delta = 0.5$) in $Sr_2FeO_{4-\delta}$. In other words, the system transforms from a partially delocalized to a fully localized one. The exchange-correlation functional is important for the correct description of such subtle electronic effects. Tables S13 and S14 of Ref. [39] summarize test calculations spanning a U_{eff} range form 2.5–6.0 eV and also compare to the Heyd-Scuseria-Ernzerhof screened hybrid functional (HSE06 [40]). While the splitting between spin-up and spin-down states increases with larger U_{eff} values as expected, lattice parameters and the shape of the DOS remain largely identical. For Sr_2FeO_4, the Fe magnetic moment μ_{Fe} shows a slight variation with U_{eff} by $\pm 0.1\ \mu_B$ (possibly related to the change in the shortest Fe-O length), but this variation by $0.1\ \mu_B$ is small compared to the overall μ_{Fe} range (discussed in Sec. III B). The shape of the DOS from HSE06 is quite similar to that from the PBE + U_{eff} calculations, with one small difference: The exact position of the Fermi level is higher with HSE06 (0.5–1.0 eV), thus when plotting the DOS aligned to $E_{\text{Fermi}} = 0$ the HSE06 results appear shifted to lower energy by 0.5–1.0 eV compared to PBE + U_{eff}. (De-)localization and Fe-O covalency in Sr_2FeO_4 vs. $SrFeO_3$ are discussed in more detail in Sec. III E.

TABLE I. Main computational parameters.

Computer code	VASP 6.1.2	
Cutoff energy	520 eV	
Space group (SG), Settings	64, *Bbem*	139, *I4/mmm*
Transformation matrix of crystallographic unit cell to supercell	$\begin{pmatrix} 1 & 1 & 0 \\ -1 & 1 & 0 \\ 0 & 0 & 1 \end{pmatrix}$	$\begin{pmatrix} 2 & 0 & 0 \\ 0 & 2 & 0 \\ 0 & 0 & 1 \end{pmatrix}$
K points	Monkhorst-Pack [44] $4 \times 4 \times 2$	
Exchange-correlation functional	Perdew-Burke-Ernzerhof [45]	
U_{eff}	4.0 eV	
Residual external pressure	<1 kbar	
Forces on atoms	<0.02 eV/Å	

The main computational parameters are listed in Table I. The effect of core electrons has been substituted by the projector augmented-wave (PAW) method of Blöchl *et al.* [41] and the ultrasoft pseudopotentials (US-PP) method of Vanderbilt [42], resulting in the so-called PAW potentials as implemented in VASP [43] (Table II).

Spin polarization has been taken into account, focusing on the FM solution; all Fe^{4+} cations were set into the high spin state. While it is important not to neglect spin polarization, the particular magnetic order practically does not affect either formation or migration energies (as long as the order does not change). The FM solution is less prone to artificial energy deviations due to the defect-induced spin reorientation. The

TABLE II. Projector Augmented-Wave (PAW) Perdew-Burke-Ernzerhof (PBE) [45] potentials for core electrons effect.

Potential	Valence electrons	E_{cutoff} (eV)
Sr	$4s^2 4p^6 5s^2$	229.353
Fe	$3d^7 4s^1$	267.883
O	$2s^2 2p^4$	400.000

total spin in the supercell was fixed accordingly. Analysis of atomic charge as well as the z component of magnetic moment (hereafter, the magnetic moment) has been calculated topologically from the spin density [46].

The structure of the system with oxygen vacancies has been completely reoptimized with no symmetry restrictions, including the lattice parameters. Optimized lattice constants and the atomic coordinates are given in Sec. I of Ref. [39].

Oxygen vacancy formation is considered in a neutral supercell as follows:

$$Sr_2FeO_4 \rightarrow Sr_2FeO_{4-\delta} + \delta\tfrac{1}{2}O_2. \quad (1)$$

Normalized by δ, the vacancy formation energy has been calculated relative to the experimental O_2 binding energy value of 5.16 eV [47]:

$$E_{\text{form}.\delta} = \frac{1}{\delta}(E_\delta + \delta(E_O + {}^1/_2 E_{\text{bind}}) - E_{\delta=0}), \quad (2)$$

where E_δ is the calculated energy of the system with oxygen nonstoichiometry δ, E_O is thecalculated energy of an isolated oxygen atom, E_{bind} is the experimental binding energy of O_2 molecule, $E_{\delta=0}$ is the calculated energy of the ideal material calculated in its lowest energy structur—orthorhombic structure (SG 64).

In the first-order RP phase, one octahedral perovskite-like layer (ABO_3) alternates with a rocksalt-type layer (AO) (Fig. 1).

It has been experimentally observed [48] that Sr_2FeO_4 crystallizes in the tetragonal structure (SG 139) in a broad temperature range. However, magnetic structure experiments revealed an elliptical cycloidal spin spiral below the Nèel temperature of 56 K, which is incompatible with the tetragonal structure (SG 139), as mentioned in Ref. [49] and discussed in more detail by us in Ref. [50]. In the present study, we address the lower symmetry structure of Sr_2FeO_4 (SG 64) since its energy as a reference affects the calculated defect formation energies. Introduction of a defect brings the system into a low symmetry state, the total energy of the perfect system needs to be calculated in the low-symmetry state, too (in particular if small defect formation energies are concerned [32]). The structure of Sr_2FeO_4 (SG 64) comprises two inequivalent and thus chemically different oxygen sites (and, therefore, oxygen vacancies): apical O_{ap} [Wyckoff position (WP) $8d$] in the SrO plane between Sr and Fe, and equatorial O_{eq} (WP $8f$) in the FeO_2 plane between the two Fe. Both are present at equal concentrations—$Sr_2FeO_{ap2}O_{eq2}$. We use the following notation to distinguish two types of oxygen vacancies in the system: Sr-$V_O^{\bullet\bullet}$-Fe and Fe-$V_O^{\bullet\bullet}$-Fe.

Although it is common in the literature to refer to them as "in SrO-" and "in FeO_2-layer" vacancies, we prefer to emphasize both neighboring cations in the nomenclature. For

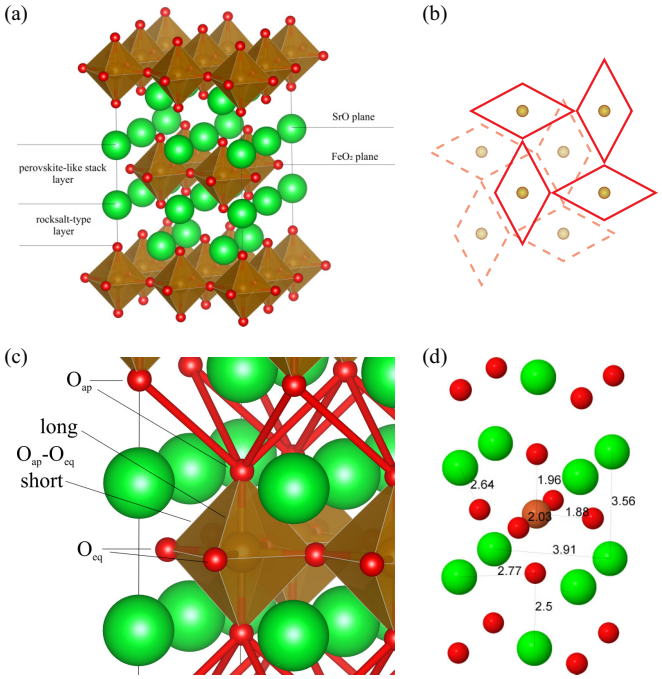

FIG. 1. (a) The model supercell of Sr_2FeO_4 Ruddlesden-Popper $n = 1$ phase (SG 64). Green: Sr, dark yellow: Fe, red: oxygen (visualization by VESTA [51]). (b) Schematic (exaggerated) view of oxygen rhombi distortion in two FeO_2 basal planes (solid and dashed lines) of the suprecell as calculated in SG 64. (c) Four types of inequivalent O-O distances: $O_{ap} - O_{ap}$, $O_{eq} - O_{eq}$, long and short $O_{ap} - O_{eq}$. Oxygen vacancy migration occurs along these four types of bonds. (d) Interatomic distances in the ideal structure (SG 64), in Å.

a detailed analysis, the total oxygen nonstoichiometry δ is split into partial values for each type of vacancy–$\delta_{Sr-V_O^{\bullet\bullet}-Fe}$ and $\delta_{Fe-V_O^{\bullet\bullet}-Fe}$. ($\delta_{Fe-V_O^{\bullet\bullet}-Fe} \equiv \delta - \delta_{Sr-V_O^{\bullet\bullet}-Fe}$) So the general formula $Sr_2FeO_{4-\delta}$ transforms into the type-specific version of it: $Sr_2FeO_{ap.2-\delta_{Sr-V_O^{\bullet\bullet}-Fe}}O_{eq.2-\delta_{Fe-V_O^{\bullet\bullet}-Fe}}$

B. Spatial $V_O^{\bullet\bullet}$ configurations

For defect calculations using the transformation matrix (Table I), a supercell comprising eight Sr_2FeO_4 formula units has been created, which is used for all calculations. The size of the $Sr_{16}Fe_8O_{32}$ model supercell is sufficient for simulating noninteracting single defects (it can also be taken as reference states for defect interaction energy calculations, described below). The lowest possible oxygen nonstoichiometry for such a supercell is $\delta = 0.125$. The smallest distance between the periodic images of Sr-$V_O^{\bullet\bullet}$-Fe and Fe-$V_O^{\bullet\bullet}$-Fe oxygen vacancy in the model supercell is 9 NN and 8 NN, by $O_{ap}-O_{ap}$ and $O_{eq}-O_{eq}$ NN list, respectively. For higher values of δ the *Supercell* program [52] has been used, which applies atoms enumerative combinatorics to find *all* structurally inequivalent defect configurations for a given value of δ. Defining the nonstoichiometry of each vacancy type – $\delta_{Sr-V_O^{\bullet\bullet}-Fe}$ and $\delta_{Fe-V_O^{\bullet\bullet}-Fe}$, a set of unique configurations has been generated. The contribution of each configuration into the pool for a particular value of δ has been calculated, yielding 2, 19, 482 configurations for $\delta = 0.125$, 0.25, and 0.5, respectively. These numbers of configurations for each δ are based fully

on the symmetry information about the supercell, resulting in a complete set of all energy states with a corresponding contribution weight. Similar analysis and approaches were used to study oxygen vacancies behavour at different δ in (Ba, Sr)$FeO_{3-\delta}$ [8], γ-Fe_2O_3 [53], and Pr distribution in $(Sr_{1-x}Pr_x)_2FeO_{4\pm\delta}$ [35]. More details are given in Sec. II of Ref. [39]. For generation of inequivalent configurations by the *Supercell* [52] code the undistorted structure (high-symmetry tetragonal SG 139) has been used. The vacancy-induced distortions will prevail over that in SG 64. It has been proven for $\delta = 0.25$ that geometry optimization reduces the number of inequivalent solutions from 28 based on SG 64 to the actual number of 19 inequivalent configurations derived from the undistorted structure (SG 139). More details are given in Sec. III of Ref. [39].

Alternatively, the special quasirandom structures (SQS) method for the supercell model or coherent potential approximation (CPA) method [54] is also widely used in the literature for defect formation and electronic structure properties of disordered systems (disordering mainly concerns the cation sublattice in Refs. [55–57]). If randomness is an important characteristic, the supercell size should be typically increased for one δ value. The SQS method is well suited for defects in high-entropy materials [56,58]. However, here we rely on the fact that most of the perovskite-type oxides containing A^{2+} cations such as $SrFeO_{3-\delta}$, $BaFeO_{3-\delta}$ exhibit large δ values and a tendency for oxygen vacancy ordering with the growth of δ. Thus, we prefer to calculate ground-state structures for a set of symmetry-derived configurations, varying δ from 0 to 0.5, reflecting also possible ordering effects.

Selection of particular configurations for a detailed analysis is done based on specific criteria. It is common to select particular configurations based on the energy of the system. For some properties, however, it would be beneficial to consider other details, e.g., the probability of observing a particular defect configuration. This is addressed in Sec. V of Ref. [39]. Despite favorable energy, a configuration can be extremely rare, therefore only marginally contributing for a realistic description of the system under study. Another criterium to consider is the interdefect distance. Multiple point defects within the supercell may create extended defects, which may reduce the total energy. Interdefect distance is also important for tracing the electronic properties depending on defect concentration, e.g., point defect induced electron charge redistribution as discussed later. Interdefect distances can be obtained from the configurational matrices, generated by the Mastrikov-Koch method [59] (see Sec. IV of Ref. [39]).

Some configurations created automatically, as well as appearing during geometry optimization, may exhibit a very unusual structure (atoms significantly shifted from their original positions, oxygen displaced into initially vacant sites, etc.). Such changes can be monitored by calculating the displacement vector, as suggested by Henkelman [60]. This parameter indicates whether the configuration still can be considered the same structure or it has transformed into something different (e.g., extended defects, clusters of defects). Without such an analysis, considering the energy state only, there is a significant risk to take a system completely different to the original structure as a legit solution, in particular, at high defect concentration (see Sec. VI of Ref. [39]). So, in addition to the total energy, other significant factors could be taken into account for tracing properties of the system, depending on the defect concentration.

C. Modelling of anti-Frenkel defects

The oxygen interstitial was introduced in the form of an anti-Frenkel pair. Thus, it is charge compensated by an oxygen vacancy $V_O^{\bullet\bullet}$. For denoting the interstitial sites, we use the WPs in SG 64. WPs in this context are meant to indicate a particular position relative to other atoms in the structure (not for populating all equivalent sites). Interstitial oxygen has been placed in four positions: "double-occupancy" between two Fe cations (WP "8*f*" in SG 64) and between Fe and Sr cations ("8*d*"), hollow position between two Sr cations ("4*b*", FeO_2 plane), tetrahedral position between four Sr cations ("8*e*"), cf. Fig. 6(b). In the calculated configurations, the distance between O_i'' and $V_O^{\bullet\bullet}$ is chosen to be the largest possible in the model supercell. Relaxation of the anti-Frenkel defect configurations leads to the formation of O_2^{2-}, O_2^{n-} complexes or atomic oxygen interstitials O_i^{2-} (more details in Sec. III E). However, we still use these notations by putting them in quotes for the sake of convenience.

D. Defect migration barriers

Oxygen vacancy and interstitial migration have been modelled by means of climbing nudged elastic bands (CNEB) [61], using nine intermediate images. The lattice basis in both terminating states is the same as that in the ideal bulk. Test calculations showed that such a constraint has a negligible effect on the calculated activation energy value in this system. The RP structure implies four inequivalent O-O distances: long and short O_{ap}–O_{eq}, O_{eq}–O_{eq} and O_{ap}–O_{ap} bond [Fig. 1(c)]. Migration barriers are obtained for $\delta = 0.125$, which eliminates the interaction of migrating oxygen with other defects (except vacancy's own periodic images in the supercell). As shown below, the calculated migration profiles for oxygen interstitial and vacancy can be asymmetric due to anisotropy and/or the presence of other defects (anti-Frenkel pair). We apply the approach of Kinetically Resolved Activation barrier (KRA) [38,62–65], which calculates the effective barrier as the average of the forward and backward barriers:

$$\Delta E_{\mathrm{KRA}} = E_{TS} - \tfrac{1}{2}(E_{T1} + E_{T2}), \tag{3}$$

where E_{TS}, E_{T1}, E_{T2} are transition (TS) and terminating (T1, T2) state energies.

III. RESULTS AND DISCUSSION

A. Sr_2FeO_4: the ground-state structure

The energetically most stable structure of Sr_2FeO_4 is found to be in the orthorhombic SG 64 [*Bbem* settings, Figs. 1(a) and 1(d)] by the present DFT + U_{eff} calculations (lower by 13 meV/f.u. compared to SG 139), as well as the WC3PW hybrid functional calculations [50] employing a Gaussian-type basis in CRYSTAL23 [66]. If this symmetry lowering was neglected for the stoichiometric Sr_2FeO_4, it would nevertheless unavoidably occur for oxygen-deficient cells that have decreased symmetry, and this will artificially decrease

TABLE III. Comparison of interatomic distances in optimized ideal distorted (SG 64, *Bbem*) and undistorted (SG 139, *I4/mmm*) structure, in angstroms.

Ion		Bond orientation relative to the basal plane	SG/Settings 64/ *Bbem* [Fig. 1(d)]	139/ *I/4mmm*
Fe	O_{ap}		1.96	1.97
Fe	O_{eq}		1.88	1.95
Fe	O_{eq}		2.03	–
Sr	Sr	normal	3.56	3.58
Sr	Sr	in plane	3.91	3.89
Sr	O_{ap}	normal	2.50	2.52
Sr	O_{ap}	in plane	2.77	2.76
Sr	O_{eq}		2.64	2.64

the $V_O^{\bullet\bullet}$ formation energy by $\approx 8 \cdot 0.013$ eV ≈ 0.1 eV, which is not negligible.

In this phase, the structure exhibits a proper as well as a pseudo JT effect [67,68] consistent with the corresponding irreps products [50]. The simultaneous presence of two types of JT effect [68] is not surprising since anti-bonding $\sigma^* - A_{1g}$ and $\sigma^* - B_{1g}$ crystal orbitals (around the Fermi energy) and degenerate $\pi^* - E_g$ crystal orbitals (3 eV lower) are occupied by unpaired Fe $3d$ electrons in a tetragonal crystal field (SG 139, I4/mmm). Besides, the latter crystalline orbital is very close in energy with the antibonding nondegenerate $\pi^* - B_{2g}$ crystalline orbital. The dominating vibrational instability mode is X_2^+ (b_{1g}) leading to a rhombic relaxation pattern within the FeO_2-plane [Fig. 1(b)], giving rise to two different Fe$-O_{eq}$ bond lengths (Table III). At the same time, all Fe$-O_{ap}$ bonds are forced by the symmetry to have the same length [Fig. 1(d)]. Symmetry also gives equal magnetic moments and charges of Fe cations in the ground-state structure.

As shown in Ref. [50], hybrid functional calculations yield three more metastable states of different symmetry. The tetragonal phase can be characterized by shortened and enlarged lattice parameters within and normal to the basal plane, relative to the SG 64 structure (Table S1 of Ref. [39]). Thus, we have shown the presence of the JT distortion around the Fe^{4+} cations in the ideal Sr_2FeO_4, leading to the symmetry reduction to orthorhombic (SG 64) [50]. The phase transition from the tetragonal (SG 139) to orthorhombic (SG 64) structure in Ln_2NiO_4 is known experimentally [69,70], and was related there to a decrease in the oxygen partial pressure.

The calculated magnetic moment (μ_{Fe}) of Fe^{4+} in the ideal Sr_2FeO_4 is 3.67 μ_B, being smaller than the formal value of 4 μB ($3d^4$) for the high-spin state. During the electronic structure optimization, most of the spin density is localized on Fe (Fig. 2), whereas the rest is predominantly distributed between O_{eq}. This is in part caused by the typical overestimation of covalence by DFT. In oxides, iron Fe^{3+}, Fe^{4+} is typically in a high-spin configuration, as found also in (Ba, Sr)FeO_3 [71] and Sr_2FeO_4 [48] from magnetic experiments.

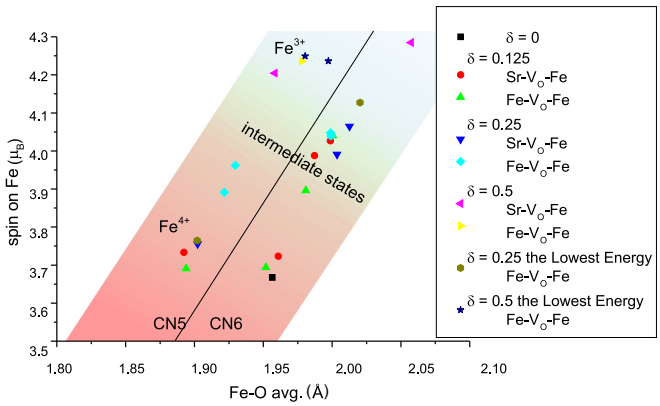

FIG. 2. Assignment of Fe oxidation states in $Sr_2FeO_{4-\delta}$, based on the magnetic moment and averaged Fe-O bond lengths, for the cases listed in Table IV, including the lowest-energy configurations for $\delta = 0.25$ and 0.5. The solid line denotes the border between Fe with fivefold (CN5) and sixfold (CN6) oxygen coordination.

B. $Sr_2FeO_{4-\delta}$

Oxygen vacancies have been created by removing a neutral oxygen atom from the system. In perovskite-type materials, an oxygen vacancy is usually compensated either by doping or by the change of the oxidation state of the *B* cation. In particular, Sr_2FeO_4 represents a negative charge transfer material, cf. electronic DOS (Fig. S1 of Ref. [39]).

$$O_O^x + 2Fe_{Fe}^x \leftrightarrow \tfrac{1}{2}O_2 + V_O^{\bullet\bullet} + 2Fe_{Fe}^{'}, \tag{4}$$

where $Fe_{Fe}^x = Fe^{4+}$ and $Fe_{Fe}^{'} = Fe^{3+}$. This reaction comprises the neutral material in oxidized and in oxygen-deficient state and, thus, automatically takes care of related Fermi level change and fulfillment of the electroneutrality condition.

Two electrons of each removed oxygen redistribute within the supercell and give rise to a lower iron oxidation state (and to a smaller degree of oxygen reduction), as demonstrated for many ABO_3 systems [72]. Owing to the additional *A*O layers in the RP phase, the behavour of the electron density upon oxygen removal may differ somewhat from simple ABO_3 systems. Moreover, literature so far did not analyzed the electron density redistribution in $Sr_2FeO_{4-\delta}$, which is critical for a deeper understanding of defect behavour and energetics. Here we suggest such an analysis. Based on Eq. (4), the states of Fe cations are expected to be

$$Sr_2\left(Fe_{1-2\delta}^{4+}Fe_{2\delta}^{3+}\right)O_{3-\delta}. \tag{5}$$

All inequivalent geometry configurations of $V_O^{\bullet\bullet}$ for a given δ have been identified and calculated. The electron redistribution caused by the removal of one neutral O predominantly occurs to iron cations, formally reducing two Fe cations from 4+ to 3+ state. Depending on the computational method, the degree of localization of these two electrons may vary, making it difficult to distinguish between these formal oxidation states. No strong correlation between the calculated (Bader) charge and the oxidation state has been observed (cf. Table S11 of Ref. [39]). To identify the oxidation state in the present DFT+*U* approach, we mainly analyze magnetic moment, Fe-O coordination number (CN), and Fe-O bond lengths. Iron in the formal 3+ state is expected to have a larger spin (d^5

configuration, formal $\mu_{Fe} = 5\,\mu_B$) and extended Fe-O bonds. It is important to include the CN in the analysis, because the data in Table S11 and Fig. 2 show a clear offset between Fe in fivefold and sixfold coordination (a smaller CN leads to a decreased average bond length, similar as in $BaFeO_{3-\delta}$ [38]). While alone none of these parameters clearly identifies the Fe oxidation state, in combination they provide a solid basis for the *oxidation state mapping*.

To identify reference points for such a mapping, we first focus on configurations in which the $V_O^{\bullet\bullet}$ have as large as possible distances (listed in Table S11 of Ref. [39]) so that the assignment of Fe oxidation states is least affected by neighboring defects. As the oxygen nonstoichiometry δ grows, the largest possible interdefect distance decreases, and naturally an overlap occurs between the electron density perturbation patterns. Nevertheless, boundaries and a transition zone between the formal Fe oxidation states can be identified as demonstrated in Fig. 2.

For Sr-$V_O^{\bullet\bullet}$-Fe as well as Fe-$V_O^{\bullet\bullet}$-Fe in $Sr_2FeO_{3.875}$, the largest negative extra charge is observed on the Fe cation(s) nearest to the $V_O^{\bullet\bullet}$. However, this does not necessarily indicate the switch to the 3+ state, because two other Fe have higher magnetic moments (4.03 and 4.04 μ_B) and clearly larger equatorial as well as overall Fe-O lengths than other 6-fold coordinated Fe. Thus, in these configurations these two Fe cations are assigned as Fe^{3+} (as formally required for one $V_O^{\bullet\bullet}$). Also, for $\delta = 0.25$, the Fe^{3+} characterized by $\geqslant$4.04 μ_B and large Fe-O $\geqslant$2.00 Å (for CN = 6) are found only in the second sphere relative to the oxygen vacancy. For $\delta = 0.5$, all Fe cations are expected to be in the 3+ state, exhibiting large magnetic moments ($\geqslant$4.20 μ_B) as well as large Fe-O bonds ($\geqslant$1.98 Å for CN = 5).

While overall the map in Fig. 2 allows one to identify most of the formal Fe oxidation states, still some data (in particular some Sr-$V_O^{\bullet\bullet}$-Fe cases) fall into the zone of intermediate states, which can be attributed to a delicate balance of the degree of localization. While we expect that a similar mapping technique can also be applied for other materials (or calculated with different functionals), the exact boundaries will differ and need to be validated. A striking result of the oxidation state assignment in $Sr_2FeO_{4-\delta}$ is that the Fe with $V_O^{\bullet\bullet}$ in the first coordination shell are in 4+ oxidation state, in contrast to the naive expectation from electrostatic interaction, which would predict Fe^{3+}. But the presence of a $V_O^{\bullet\bullet}$ in the first coordination sphere of Fe^{4+} can be regarded as a special case of JT distortion (absence of one O instead of elongation of two Fe-O bonds), thus stabilizing this configuration. The identification of Fe oxidation states in $Sr_2FeO_{4-\delta}$ is also important for the investigation of protonated materials, since, for example, of $BaFeO_{3-\delta}$ the proton affinity of different oxide ions in a defect-containing supercell has been found to be sensitive the Fe oxidation state as well as to the position relative to a $V_O^{\bullet\bullet}$ [8].

C. Dependence of vacancy formation energy and volume on δ.

Comparing the vacancy formation energies at $\delta = 0.125$ in SrO and FeO_2 planes, the latter appear to be energetically slightly more favorable ([Table S8] of Ref. [39], Fig. 3), which is in agreement with experimental work [27]. Also, for higher

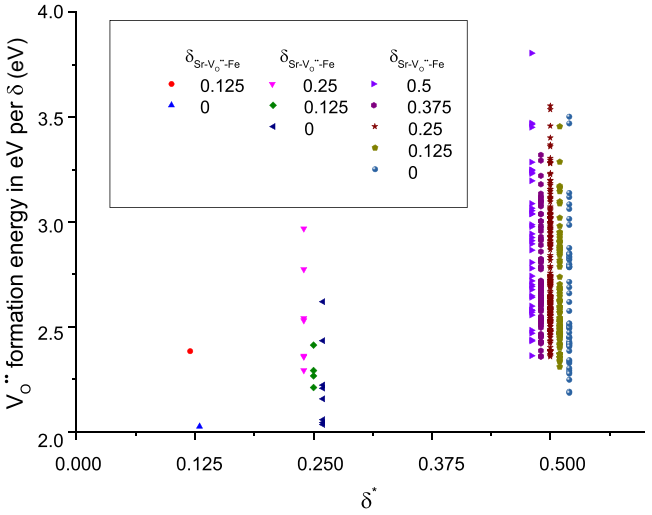

FIG. 3. Oxygen vacancy formation energy per δ (relative to O_2) [Eq. (2)]. Multiple data for the same δ value correspond to various spatial distributions of the defects. For better readability, data points are displayed according to the adjusted value of $\delta^* = \delta + 0.04\ (\delta - 2\delta_{Sr-V_O^{\bullet\bullet}-Fe})$.

δ values, the lowest formation energy values correspond the $\delta_{Fe-V_O^{\bullet\bullet}-Fe} = \delta$ cases. This is an interesting and important observation. Intuitively, one might have expected easier $V_O^{\bullet\bullet}$ formation for the Sr-$V_O^{\bullet\bullet}$-Fe case, because the O to be removed has only one Fe-O bond (which is considered stronger than Sr-O one). Also, the higher center of gravity of the Sr-O oxygen states in the electronic density of states ([Fig. S1] of Ref. [39]) should be in favor for removing an O from the SrO layer, cf. [73] for ABO_3 perovksites. However, the $V_O^{\bullet\bullet}$ formation energy is not only affected by the initial but also by possible stabilization effects in the final state. Two contributions favor Fe-$V_O^{\bullet\bullet}$-Fe over Sr-$V_O^{\bullet\bullet}$-Fe case and together can explain the preference of Fe-$V_O^{\bullet\bullet}$-Fe. (I) upon removal of O, the opposite Fe-O bond is shortened (by approx. 0.14 Å) and strengthened. For the Sr-$V_O^{\bullet\bullet}$-Fe case, this can happen only at one Fe, while for Fe-$V_O^{\bullet\bullet}$-Fe, it occurs at both Fe neighboring the $V_O^{\bullet\bullet}$. (II) As discussed before, the presence of a $V_O^{\bullet\bullet}$ in the first coordination sphere of Fe^{4+} can be regarded as an extreme case of JT distortion, and for the Fe-$V_O^{\bullet\bullet}$-Fe case, two Fe cations can benefit from such a JT stabilization.

The energetically most favorable solutions demonstrate an extremely low dependency on oxygen nonstoichiometry $\delta \leqslant 0.5$, ranging from 2.0 to 2.4 eV (Table S8). Again, for a consistent analysis, the total energy of a particular configuration alone is not enough; the structure of the relaxed system has to be examined as well (within the $\delta_{Fe-V_O^{\bullet\bullet}-Fe} = \delta$ cases, the increase is only from 2.0 to 2.2 eV). This very low dependence on δ is in a stark contrast with the results for the regular perovskite phase. In $SrFeO_{3-\delta}$ the oxygen vacancy formation energy depends strongly on oxygen nonstoichiometry (increase by 1.5 eV when moving from $\delta = 0.125$ to 0.5, i.e.,still staying in the regime between Fe^{4+} and Fe^{3+}) [74]. In $BaFeO_{3-\delta}$ a similar increase from 0.2 to 1.6 eV is found [8]. This could be attributed to relatively higher delocalization in the regular perovskite phase in comparison to RP.

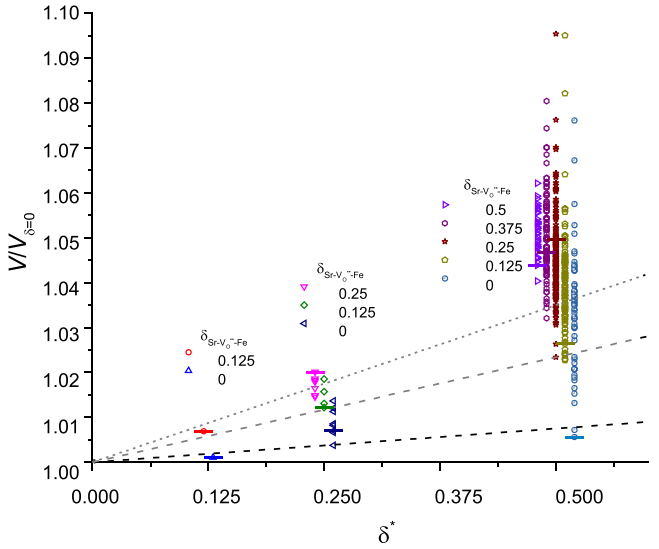

FIG. 4. Dependence of volume on oxygen nonstoichiometry δ^*, relative to the volume of the ideal material. For better readability, data points are displayed according to the adjusted value of $\boldsymbol{\delta^* = \delta + 0.04(\delta - 2\delta_{Sr-V_O^{••}-Fe})}$. Black dash, gray dash, and gray dot lines connect the lowest energy states (marked with dashes) of $\boldsymbol{\delta_{Sr-V_O^{••}-Fe}/\delta}$ equal to 0, 0.5, and 1, respectively.

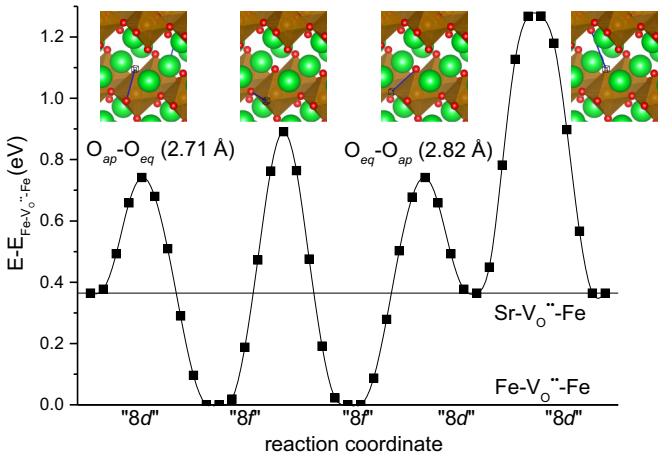

FIG. 5. Oxygen vacancy migration barriers. Four unique barriers via O_{ap}−O_{eq} short, O_{eq}−O_{eq}, O_{eq}−O_{ap} long, and O_{ap}−O_{ap} bond. Zero level corresponds to the Fe-$V_O^{••}$-Fe vacancy state. The position of the vacancy is denoted by the nearest Wyckoff position in SG 64. The KRA barrier values are (from left to right): 0.56, 0.89, 0.56, and 0.90 eV.

When treating hundreds of configurations, it is worthwhile to calculate also the probability to find the system in a particular energy state for a given value of δ. Such an analysis is performed in [Sec. V] of Ref. [39].

There is a consistent volume increase from smaller to larger values of δ (Fig. 4). The most significant volume growth is due to the presence of Sr-$V_O^{••}$-Fe-type vacancies. Even at the lowest partial $\delta_{Sr-V_O^{••}-Fe}$, the average volume is significantly larger in comparison to $\delta_{Sr-V_O^{••}-Fe} = 0$ configurations. This can be understood from the fact that the average bond strengths in the direction normal to the basal plane are weaker, and correspondingly, this direction shows a larger expansion. For the Fe-$V_O^{••}$-Fe case, the broken Fe-O bonds are in the basal plane, which is less susceptible to respective lattice parameter expansion. In Fig. 4, the guidelines for the configurations with only Fe-$V_O^{••}$-Fe indicate that for the low-energy configurations the volume increase with δ is approximately linear. Up to $\delta = 0.25$, this holds also for the other $V_O^{••}$ configurations. For large $\delta = 0.5$ together with Sr-$V_O^{••}$-Fe contributions, many configurations are close in energy but show significant volume variation. This makes it ambiguous to extend the correlation lines in Fig. 4 to $\delta = 0.5$. Only for all-Fe-$V_O^{••}$-Fe, two configurations have clearly lower energy than the others (dominant contribution), and thus the dashed line is extended there. For comparison the volume expansion ("chemical expansion") and $V_O^{••}$ formation energies in other perovskite-type materials are given in Table IV. Overall, the tendency for decreased chemical expansion can be understood from the fact that the RP phase contains a larger fraction of redox-inactive SrO relative to FeO_2. Only the contribution from the Sr-$V_O^{••}$-Fe in RP $Sr_2FeO_{4-\delta}$ is comparable to that for oxygen vacancies in $SrFeO_{3-\delta}$.

D. Oxygen vacancy migration

In perovskite-type materials, oxygen migration occurs from an occupied to an unoccupied regular O site through the *A-B-A critical triangle* [80], keeping one *B*-O bond also in the transition state. In general, the larger the open space in the *critical triangle*, the lower is the activation barrier. In addition to that mechanism, in the RP phase an oxygen vacancy can also migrate between two *A* cations from one to the neighboring *A*-O plane, which corresponds to a slightly larger jump distance. The presence of $V_O^{••}$ sites with different energy leads to a complex energy landscape with asymmetric barriers.

The obtained migration barriers suggest the energetically most favorable path is along O_{ap}−O_{eq} [Fig. 1(c)]. This barrier has the largest Sr-Sr distance of 3.91 Å (i.e. large open space within the critical triangle) and a height of $\Delta E_{KRA} = 0.58$ eV. Owing to the shorter Sr-Sr distance of 3.56 Å, O_{eq}−O_{eq} jumps within the FeO_2 plane require more energy ($\Delta E_{KRA} = 0.89$ eV). Thus migration parallel to the FeO_2 plane occurs in a zigzag manner via the the O_{ap}−O_{eq} paths. Although it involves the higher-energy O_{ap} position, this path leads to a higher overall $V_O^{••}$ conductivity because the maximum in the energy profile along this path is lower than for the O_{eq}−O_{eq} path (Fig. 5).

O migration within the SrO layer between two O_{ap} positions also has a high barrier of 0.9 eV. This high barrier can be attributed to the fact that in the transition state the only existing Fe-O bond is broken (for O_{eq}−O_{eq} and O_{ap}−O_{eq} barriers, one out of two Fe-O bonds remains and can be strengthened).

E. Discussion of the Fe-O bonding character

The present calculations for Sr_2FeO_4 with the Ruddlesden-Popper structure indicate some characteristic differences in the Fe-O bonding in Sr_2FeO_4 compared to the $SrFeO_3$ simple perovskite, despite formally having iron in 4+ oxidation state in both materials. We want to discuss these differences based

TABLE IV. Chemical expansion and $V_O^{\bullet\bullet}$ formation energies (by neutral O removal) in perovskite-type materials from DFT+U calculations. Typical experimental values of chemical expansion in simple ferrate perovskites are 11% for $SrFe_{0.75}Ti_{0.25}O_{3-\delta}$ and $La_{0.3}Sr_{0.7}FeO_{3-\delta}$ [75,76].

Material	Volume expansion (%)	Formation energy (eV)
$Sr_2FeO_{4-\delta}$ (this study)	Sr-$V_O^{\bullet\bullet}$-Fe: 7 (∼linear) Fe-$V_O^{\bullet\bullet}$-Fe: 2 (∼linear)	Sr-$V_O^{\bullet\bullet}$-Fe: 2.0–2.2 Fe-$V_O^{\bullet\bullet}$-Fe: 2.4
$SrFeO_{3-\delta}$ [72]	–	0.4−∼ 1.5[a]
[74]	6.6 (linear)	0.5–1.7[a]
$La_{0.5}Sr_{0.5}FeO_{3-\delta}$ [32]	14 (linear)	0.55
$Ba_{0.5}Sr_{0.5}FeO_{3-\delta}$ [8]	7.6 (linear)	0.30–1.73[a]
$BaFeO_{3-\delta}$ [8]	9 (linear)	0.22–1.70[a]

[a]These values were not corrected for the DFT overbinding in the O_2 molecule (a correction would increase the $V_O^{\bullet\bullet}$ formation energy by about 0.6–0.7 eV [8,72] if the experimental data for O_2 from Ref. [77] is used to account for the (room) temperature effect [78,79]).

on properties that can easily be extracted from DFT calculations (cf. Tables S13, S14 and Fig. S6–S8 of Ref. [39]).

The first aspect is related to the geometry. Iron with formal 4+ oxidation state has a high-spin $3d^4$ orbital occupation and should in principle develop a JT-type distortion. This is observed in Sr_2FeO_4, where actually three different Fe-O bond lengths are found (1.88 and 2.03 Å in the equatorial plane; the apical distance of 1.96 Å is also clearly longer than the shortest Fe-O but modified by the fact that it points into the rocksalt-structured layer). In contrast, $SrFeO_3$ is perfectly cubic with only one Fe-O length of 1.94 Å. It is well established experimentally (e.g., Refs. [28,81,82]) and from electronic structure calculations (e.g., Ref. [83]) that $SrFeO_3$ has a strong transfer of electron density from the oxide anions to the iron cation ("negative charge transfer material"; "ligand hole formation"). Thus the actual orbital occupation approaches $3d^5$, and correspondingly the Jahn-Teller distortion vanishes. (Interestingly, in $BaFeO_3$ with longer Fe-O bonds (average 2.01 Å) a JT-distorted structure becomes slightly lower in energy than the ideal cubic structure [84]).

This different degree of Fe and O orbital interaction in $SrFeO_3$ also shows up in the electronic density of states and band widths (compare the DOS of $SrFeO_3$ in Fig. S6 and S_2FeO_4 in Fig. S7, and summary in Fig. S8 of Ref. [39]) where the bands in $SrFeO_3$ generally have a larger width. In $SrFeO_3$ the O states have large contributions not only close to E_{Fermi} but also in the range of Fe e_g and t_{2g} DOS at −9 to −5 eV. The Fe e_g states have perceptible DOS in the whole enregy range from −9 eV up to E_{Fermi}; correspondingly their band width is very large (Fig. S8). There is also perceptible unoccupied O DOS just above E_{Fermi}, which corresponds to the "ligand holes" from the negative charge transfer (holes in O states instead of unoccupied Fe states). In contrast, in S_2FeO_4 the O states concentrate in the region from −3 eV up to E_{Fermi} (much less overlap with Fe e_g and t_{2g}), and the O DOS just above E_{Fermi} is negligible (making S_2FeO_4 a semiconductor). The spin-up Fe e_g states have only very little DOS above −5.5 eV, resulting in a much lower band width than for $SrFeO_3$ ([Fig. S8] of Ref. [39]).

Finally, the degree of (de-)localization in the Fe-O bonds also affects the behavior of the $V_O^{\bullet\bullet}$ formation energy (removal of O according to Equation 4 in parallel to reduction with two Fe^{4+} to two Fe^{3+} per $V_O^{\bullet\bullet}$) as a function of the oxygen deficiency. In Sr_2FeO_4, the formation energy for the most stable $V_O^{\bullet\bullet}$ in the respective supercell is essentially independent of the oxygen deficiency ≈2.0 eV (Fig. 3). This corresponds to the ideal behavour of noninteracting defects. The situation in $SrFeO_3$ differs strongly: there the $V_O^{\bullet\bullet}$ formation energy is 1.2 ($Fe^{3.75+}$), 1.5 and 2.4 eV (Fe^{3+}) for $\delta = 0.125$, 0.25 and 0.5, respectively [74]. (a similar trend with $V_O^{\bullet\bullet}$ formation energy in $SrFeO_{3-\delta}$ increasing from 0.5 eV for $\delta \approx 0$ to 1.5 eV for $\delta \approx 0.5$ is found in Ref. [72] using $U_{eff} = 3$ eV). So, in $SrFeO_3$, the defects experience a strong self-interaction which disfavors further $V_O^{\bullet\bullet}$ formation. The main reason for this is not elastic strain around $V_O^{\bullet\bullet}$ or their electrostatic repulsion (the molar volume of Sr_2FeO_4 is 61% larger than that of $SrFeO_3$ corresponding to +17% linear expansion in all three space directions; thus distances between defects are in a comparable range). Rather the defect interaction is transmitted by the fact that electronic defects are much more delocalized in $SrFeO_3$ (i.e. one electronic defect affects all Fe and O in the supercell) than in Sr_2FeO_4.

All the described properties indicate that $SrFeO_3$ has much more charge transfer from O to Fe (which can also be regarded as a higher degree of covalency) and degree of delocalization than Sr_2FeO_4. We can then ask to which reasons this can be attributed. Expanded Fe-O bond lengths are probably not the main reason for the much smaller delocalization in Sr_2FeO_4 (the averaged Fe-O bond length of 1.96 Å in Sr_2FeO_4 is only marginally larger than 1.95 Å in $SrFeO_3$). The fact that Sr_2FeO_4 contains additional SrO layers with oxide ions coordinated to Sr^{2+} of low electronegativity might actually be expected to favor electron transfer from O to Fe, but the presence of the JT distortion pattern and absence of unoccupied O DOS directly above E_{Fermi} this is not the case. It appears the decisive factor is that the SrO layers break the symmetry in the bonding situation around Fe (apical vs. equatorial Fe-O, and even two different Fe-O_{eq} lengths) in a way which stabilizes quite localized Fe^{4+} states with a JT-type distortion.

IV. ANTI-FRENKEL DEFECTS

A. Interstitial sites and formation energies

The anti-Frenkel defect formation involves one oxygen vacancy and oxygen interstitial and proceeds without redox process/change of the average Fe oxidation state (the energy of the anti-Frenkel pair is given relative to the ideal bulk):

$$O_O^x + V_i^x \rightarrow V_O^{\bullet\bullet} + O_i'' . \quad (6)$$

TABLE V. Anti-Frenkel pair formation energy (E-E_{bulk}) effective charge, distance between O anions in the dumbbell configuration and between O_i'' and $V_O^{\bullet\bullet}$ in anti-Frenkel pair.

Interstitial	Type of defect	WP in SG 64, *Bbem*[a]	Vacancy type	O_i''-$V_O^{\bullet\bullet}$ distance	E-E_{bulk} (eV)	O-O distance (Å)	Charges (e)
Sr-O_2^{2-}-Fe	O_2^{2-}	"8*d*"	Sr-$V_O^{\bullet\bullet}$-Fe	6.82	2.68	1.46	−0.72(Sr)/−0.70(Fe)
		[Fig. 6(a)]	Fe-$V_O^{\bullet\bullet}$-Fe	6.07	2.17	1.46	−0.70(Sr)/−0.69(Fe)
Tetrahedral	O_i^{2-}	"8*e*"	Sr-$V_O^{\bullet\bullet}$-Fe	6.70	3.47	na	−0.99
		[Fig. 6(b)]	Fe-$V_O^{\bullet\bullet}$-Fe	6.30	3.14	na	−0.99
Fe-O_2^{n-}-Fe	O_2^{n-}	"8*f*"	Sr-$V_O^{\bullet\bullet}$-Fe	6.07	4.50	1.40	−0.61/−0.63
		[Fig. 6(c)]	Fe-$V_O^{\bullet\bullet}$-Fe	8.26	4.25	1.42	−0.65/−0.67
Hollow	O_i^{2-}	"4*b*"	Sr-$V_O^{\bullet\bullet}$-Fe	6.99	7.43	na	−0.67
		[Fig. 6(d)]	Fe-$V_O^{\bullet\bullet}$-Fe	7.60	7.08	na	−0.53

[a]WPs, relative to the conventional cell, solely for pointing out the position of interstitial.

The oxygen interstitial O_i'' can be considered in two limiting cases, namely a diatomic peroxide O_2^{2-} defect (i.e., in a regular oxygen position a peroxide group is formed) and an atomic oxide ion interstitial O_i^{2-}. We present here the results for both; the energy also depends on the type of the compensating vacancy (Sr-$V_O^{\bullet\bullet}$-Fe or Fe-$V_O^{\bullet\bullet}$-Fe) and the interdefect distance. Interstitial oxygen is energetically more stable in the SrO- rather than in the more closely packed FeO_2-layer. Energetically favorable oxygen dumbbell configurations were predicted also in other oxides, including MgO, Al_2O_3, $SrTiO_3$ [85–88], and confirmed experimentally in Al_2O_3 [89]. Oxygen interstitials will also be highly interesting as potenital sites for protonation. Owing to their nature as negative defects and long distance to highly charged Fe cations they are expected to exhibit a high proton affinity, but the detailed values will also depend on the nature andite of the interstitial defect.

The most stable oxygen interstitial configuration is the "double-occupied" Sr-O_{ap}/O*i*-Fe site [Table V, position "8*d*", Fig. 6(a)], where interstitial and regular oxygen anions O_{ap} create an O_2^{2-} dumbbell configuration. The nature of this defect can be determined on the basis of O-O interatomic distance [90] (Table V) and effective atomic charges - the interatomic distance of 1.46 Å and effective charge of ∼-1.40 e are in the typical range of peroxide anions. The tetrahedral position between the SrO planes (position "8*e*" Fig. 6b) is less stable by ∼1 eV. It corresponds to an atomic O_i species and has an effective charge of -1 e. The second meta-stable interstitial is a dumbbell in the FeO_2 plane [position "8*f*," Fig. 6(c)], i.e., formation of the O_2^{2-} peroxide group in the position of equatorial oxygen. However, it is about 2 eV less stable than the dumbbell configuration in the SrO-plane, and the effective charge of O_2^{2-} is reduced to -1.2 e. The least favorable configuration is an atomic interstitial in the hollow position within the FeO_2 plane [position "4*b*," Fig. 6(d)]. Its formation energy is about 3 eV higher than that of the least favorable dumbbell position [position "8*f*," Fig. 6(c)]. This high-energy position is structurally metastable, leading to almost zero energy barrier for the transition to the "8*f*" position (discussed below). For all interstitial configurations, a compensating Fe-$V_O^{\bullet\bullet}$-Fe vacancy is more favorable than Sr-$V_O^{\bullet\bullet}$-Fe, which is consistent with the vacancy formation energies (Table S8).

B. Migration of oxygen interstitial

In hyperstoichiometric RP materials such as $La_2CoO_{4+\delta}$ [91], transition metal doped $La_2NiO_{4+\delta}$ [65,92] and $La_{2-x}Sr_xNiO_{4+\delta}$ [93], the oxygen ion migrates easier via an interstitialcy (push-pull) mechanism within the "rock-salt" *AO*-layer than via vacancies. For oxygen-deficient RP phases, oxygen transport is due to the vacancy mechanism, e.g., in $La_{2-x}Sr_xCoO_{4-\delta}$ [94] and in $La_{2-x}Sr_xCuO_{4-y}$ ([95,96] and references therein).

In $Sr_2FeO_{4-\delta}$, we consider also migration involving O_i'' positions within the FeO_2 plane, and take into account Sr-$V_O^{\bullet\bullet}$-Fe as well as Fe-$V_O^{\bullet\bullet}$-Fe positions for the compensating $V_O^{\bullet\bullet}$ (this extends beyond the treatment in Ref. [35]). The migration

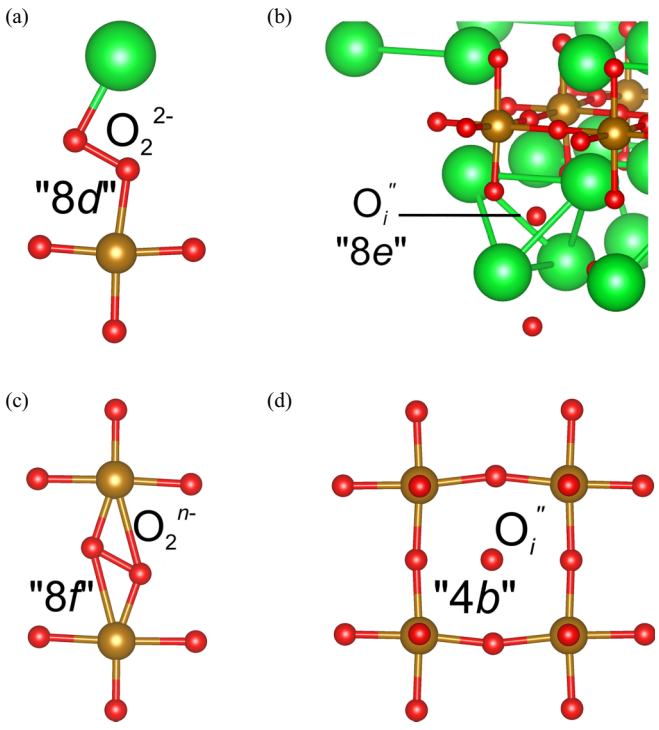

FIG. 6. Interstitial oxygen in double-occupied apical Sr-O_2^{2-}-Fe (a) and equatorial Fe-O_2^{n-}-Fe (c) positions. Tetrahedral between SrO planes (b) and hollow within FeO_2 plane (d) interstitial positions.

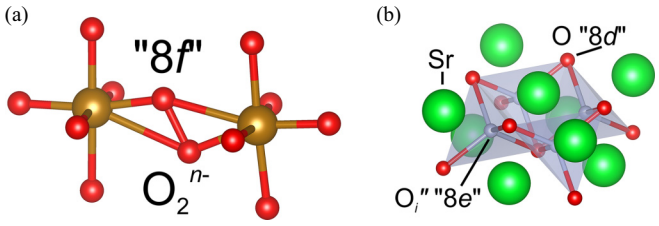

FIG. 7. (a) Oxygen interstitial O_2^{n-} at "8*f*" position, oriented perpendicularly to the basal (horizontal) plane. (b) Oxygen interstitial migration path between "8*d*" and "8*e*" sites (SrO layer).

energies of $V_O^{\bullet\bullet}$-compensated oxygen interstitial in Sr_2FeO_4 are presented relative to the ideal bulk, so the activation energy can be calculated relative to either of the two terminating states (Table S12 of Ref. [39]). We consider all possible oxygen interstitial migration between the stable configurations from Table V. Oxygen interstitial migration in $Sr_2FeO_{4-\delta}$ is a combination of translational and rotational motions, and it may or may not involve breaking the O-O bond of peroxy groups (Figs. 6 and 7).

Within the FeO_2 plane, the translational transition proceeds from one to another "8*f*" position (Fe-O_2^{n-}-Fe configuration) without O-O bond breaking and with a KRA barrier of ∼0.7 eV (left part in Fig. 8). The transition out of the FeO_2-plane into the "8*d*" position first requires rotation of the complex into an orientation perpendicular to the basal plane [Fig. 7(a), 9 top]. The translation between Fe-O_2^{n-}-Fe ("8*f*") and Sr-O_2^{2-}-Fe ("8*d*"), also occurs without O-O splitting. It is strongly asymmetric due to the total energy difference between the initial and final configuration, thus the barrier in forward direction is only 0.22 eV (KRA barrier ∼0.9 eV).

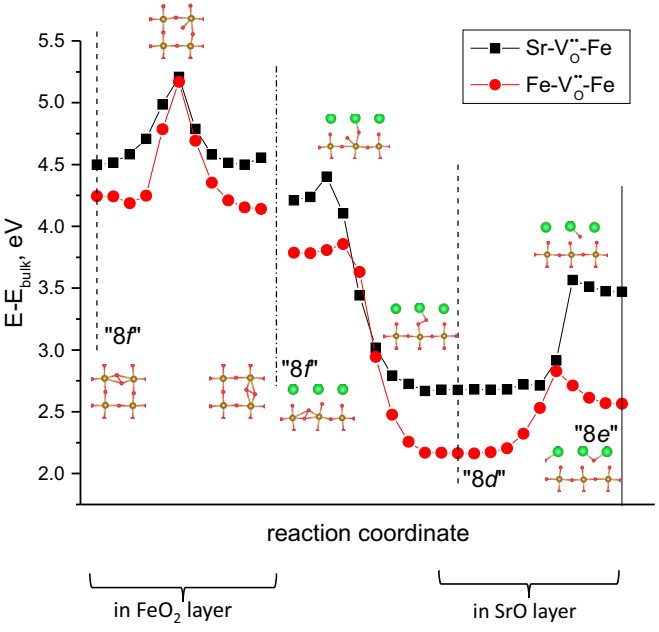

FIG. 8. Energy for oxygen interstitial migration by translational processes, relative to the ideal bulk. Two types of compensating (stationary) oxygen vacancy in the FeO_2 or SrO layer are indicated. Schematic view of the structures is given.

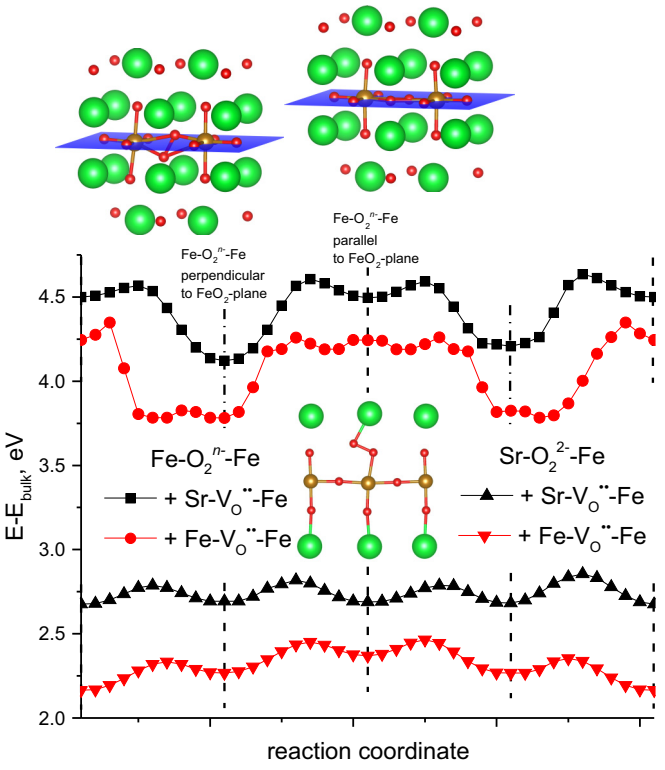

FIG. 9. O_2^{n-} complex rotational movement around the Fe-Fe (square and circle) and Sr-Fe (up and down triangle) axis, in the presence of charge-compensating Sr-$V_O^{\bullet\bullet}$-Fe (black) and Fe-$V_O^{\bullet\bullet}$-Fe (red). Energies are given relative to the ideal bulk. The defects are placed at the largest possible distance within the model cell. The rotation covers 360°.

The migration of the O interstitial within the SrO layer between "8*d*" and "8*e*" [Fig. 7(b)] involves O-O splitting. This migration proceeds from an atomic interstitial O_i^{2-} to the more stable Sr-O_2^{2-}-Fe over the barrier of 0.10 and 0.20 eV (Sr-$V_O^{\bullet\bullet}$-Fe and Fe-$V_O^{\bullet\bullet}$-Fe). In the opposite direction the barrier amounts to 0.66–0.89 eV, resulting in KRA barrier of 0.46–0.50 eV. This process of O-O bond splitting or formation is in contrast to a simple interstitialcy mechanism that involves only atomic species [65]. A difference between O_i'' migration in $Sr_2FeO_{4-\delta}$ and $La_{2-x}Sr_xNiO_{4+\delta}$ [93] lies in the higher stability of the Sr-O_2^{2-}-Fe configuration. The migration within the SrO layer also requires the "8*d*"-"8*d*" rotation(s) of the Sr-O_2^{2-}-Fe dumbbell with low barriers of 0.18 and 0.29 eV (Sr-$V_O^{\bullet\bullet}$-Fe and Fe-$V_O^{\bullet\bullet}$-Fe, Fig. 9 bottom). The jump of an atomic O interstitial from the metastable hollow "4*b*" to the "8*f*" position [Fig. 6(d)] occurs without barrier since the former is energetically very unfavorable (in line with [92]), but since this position is hardly ever occupied, this does not contribute to the long-range transport.

Overall, long-range interstitial O transport is expected to occur predominantly in the SrO layers; transport perpendicular to it is impeded by the unfavorable states of peroxy groups in the FeO_2 layer as well as by the larger barriers for translations there.

V. CONCLUSIONS

Oxygen defects in the layered $Sr_2FeO_{4\pm\delta}$ Ruddlesden-Popper phase are systematically investigated by DFT+U up to high defect concentrations $\delta = 0.5$. Interestingly, Fe^{4+} (identified from magnetic moments and Fe-O bond lengths) have a preference to be direct neighbors of $V_O^{\bullet\bullet}$. This can be explained by the fact that the presence of a $V_O^{\bullet\bullet}$ bears similarity to a Jahn-Teller distortion. The $V_O^{\bullet\bullet}$ formation energy is favored in the FeO_2 plane (Fe-$V_O^{\bullet\bullet}$-Fe 2.0–2.2 eV) compared to the SrO layer (Sr-$V_O^{\bullet\bullet}$-Fe 2.4 eV Sr-$V_O^{\bullet\bullet}$-Fe) and is almost independent of δ. This is in contrast to simple ABO_3 perovskites, which exhibit a higher degree of Fe-O bond delocalization.

Oxygen vacancy migration occurs preferentially within the FeO_2 layers via O_{ap} and O_{eq} (barrier 0.6 eV). The most favorable oxygen interstitial positions are located within and between SrO planes. A dumbbell configuration is significantly more stable than atomic O in a *hollow* position. Interstitial migration occurs within the SrO layer with a barrier of 0.5 eV and involves tetrahedrally coordinated atomic O as a transition state.

Several of the identified aspects are expected to be favorable for a protonation of $Sr_2FeO_{4\pm\delta}$ (investigated in forthcoming work). The higher Sr/Fe ratio as well as the decreased degree of Fe-O delocalization compared to the simple $SrFeO_3$ perovskite ensures a high proton affinity. The preferred location of $V_O^{\bullet\bullet}$ in the equatorial position ensures that O_{ap} in the SrO layer remains largely unaffected by the increased covalency of the Fe-O bonds opposite to the $V_O^{\bullet\bullet}$. In the electronic density of states, O states from the SrO layer have a higher center-of-gravity relative to the Fermi level than FeO_2-related states, designating them as preferred protonation sites. Therefore $Sr_2FeO_{4\pm\delta}$ proves to be a suitable model material for detailed first principles investigations of proton uptake and migration in RP-type ferrates, whereas the experimental realization focuses rather on the higher-order phases.

ACKNOWLEDGMENTS

The study was performed with the financial support from the Latvian Council of Science under the grant agreement lzp-2021/1–0203. The Institute of Solid State Physics, University of Latvia as the Centre of Excellence has received funding from the European Union's Horizon 2020 Frame-work Programme H2020-WIDESPREAD-01–2016–2017-Teaming Phase2 under Grant Agreement No. 739508, project CAMART^2. E.K. thanks the M.Era-Net (HetCat) project support. The computational resources were provided by the High Performance Computing Center Stuttgart (HLRS) under the grant DEFTD; AcID12939, the University of Maryland High-performance Computing Center and the National Energy Research Scientific Computing Center under the grant m647–DEFECTS.

DATA AVAILABILITY

The data that support the findings of this article are not publicly available. The data are available from the authors upon reasonable request.

[1] A. P. Tarutin, E. A. Filonova, S. Ricote, D. A. Medvedev, and Z. Shao, Chemical design of oxygen electrodes for solid oxide electrochemical cells: A guide, Sustain. Energy Technol. Assessments **57**, 103185 (2023).

[2] J. Cao, Y. Ji, and Z. Shao, Perovskites for protonic ceramic fuel cells: A review, Energy Environ. Sci. **15**, 2200 (2022).

[3] M. Papac, V. Stevanović, A. Zakutayev, and R. O'Hayre, Triple ionic–electronic conducting oxides for next-generation electrochemical devices, Nat. Mater. **20**, 301 (2021).

[4] R. Merkle, M. F. Hoedl, G. Raimondi, R. Zohourian, and J. Maier, Oxides with mixed protonic and electronic conductivity, Annu. Rev. Mater. Res. **51**, 461 (2021).

[5] S. N. Ruddlesden and P. Popper, IUCr. New compounds of the K_2NiF_4 type, Acta Cryst. Short Commun. **10**, 538 (1957).

[6] F. A. Kröger and H. J. Vink, Relations between the concentrations of imperfections in crystalline solids, Solid State Phys. **3**, 307 (1956).

[7] R. Zohourian, R. Merkle, G. Raimondi, and J. Maier, Mixed-conducting perovskites as cathode materials for protonic ceramic fuel cells: Understanding the trends in proton uptake, Adv. Funct. Mater. **28**, 1801241 (2018).

[8] M. F. Hoedl, D. Gryaznov, R. Merkle, E. A. Kotomin, and J. Maier, Interdependence of oxygenation and hydration in mixed-conducting (Ba, Sr)$FeO_{3-\delta}$ perovskites studied by density functional theory, J. Phys. Chem. C **124**, 11780 (2020).

[9] S. J. Skinner and J. A. Kilner, Oxygen diffusion and surface exchange in $La_{2-x}Sr_xNiO_{4+\delta}$, Solid State Ionics **135**, 709 (2000).

[10] E. Boehm, J.-M. Bassat, M. C. Steil, P. Dordor, F. Mauvy, and J.-C. Grenier, Oxygen transport properties of $La_2Ni_{1-x}Cu_xO_{4+\delta}$ mixed conducting oxides, Solid State Sci. **5**, 973 (2003).

[11] E. S. Tropin, M. V. Ananyev, A. S. Farlenkov, A. V. Khodimchuk, A. V. Berenov, A. V. Fetisov, V. A. Eremin, and A. A. Kolchugin, Surface defect chemistry and oxygen exchange kinetics in $La_{2-x}Ca_xNiO_{4+\delta}$, J. Solid State Chem. **262**, 199 (2018).

[12] C. Berger, E. Bucher, A. Egger, A. T. Strasser, N. Schrödl, C. Gspan, J. Hofer, and W. Sitte, Synthesis and characterization of the novel K_2NiF_4-type oxide $Pr_2Ni_{0.9}Co_{0.1}O_{4+\delta}$, Solid State Ionics **316**, 93 (2018).

[13] S. Eisbacher-Lubensky, A. Egger, W. Sitte, and E. Bucher, Oxygen exchange and transport properties of the first-order Ruddlesden-Popper phase $La_2Ni_{0.9}Co_{0.1}O_{4+\delta}$, Solid State Ionics **397**, 116255 (2023).

[14] C. Berger, E. Bucher, A. Egger, N. Schrödl, J. Lammer, C. Gspan, R. Merkle, W. Grogger, J. Maier, and W. Sitte, Oxygen surface exchange kinetics and electronic conductivity of the third-order Ruddlesden-Popper phase $Pr_4Ni_{2.7}Co_{0.3}O_{10-\delta}$, Solid State Ionics **348**, 115282 (2020).

[15] P. Zhong, K. Toyoura, L. Jiang, L. Chen, S. A. Ismail, N. Hatada, T. Norby, and D. Han, Protonic conduction in $La_2NiO_{4+\delta}$ and $La_{2-x}A_xNiO_{4+\delta}$ (A = Ca, Sr, Ba) Ruddlesden–

Popper type oxides, Adv. Energy Mater. **12**, 2200392 (2022).
[16] A. Grimaud, F. Mauvy, J. Marc Bassat, S. Fourcade, M. Marrony, and J. Claude Grenier, Hydration and transport properties of the $Pr_{2-x}Sr_xNiO_{4+\delta}$ compounds as H^+-SOFC cathodes, J. Mater. Chem. **22**, 16017 (2012).
[17] A. P. Tarutin, N. A. Danilov, A. A. Kalinin, A. A. Murashkina, and D. A. Medvedev, Ba-Doped $Pr_2NiO_{4+\delta}$ electrodes for proton-conducting electrochemical cells. part 1: Structure, mechanical, and chemical properties, Int. J. Hydrogen Energy **48**, 22531 (2023).
[18] E. J. Crumlin, E. Mutoro, S.-J. Ahn, G. J. la O', D. N. Leonard, A. Borisevich, M. D. Biegalski, H. M. Christen, and Y. Shao-Horn, Oxygen reduction kinetics enhancement on a heterostructured oxide surface for solid oxide fuel cells, J. Phys. Chem. Lett. **1**, 3149 (2010).
[19] Y. Chen, Z. Cai, Y. Kuru, W. Ma, H. L. Tuller, and B. Yildiz, Electronic activation of cathode superlattices at elevated temperatures–source of markedly accelerated oxygen reduction kinetics, Adv. Energy Mater. **3**, 1221 (2013).
[20] S. Stämmler, R. Merkle, and J. Maier, Oxygen exchange activity of La-Sr-Co-O PLD films and quantification of $(La, Sr)CoO_{3-\delta}/(La, Sr)_2CoO_{4+\delta}/O_2$ triple phase boundary activity, J. Electrochem. Soc. **164**, F454 (2017).
[21] Z. Wang, W. Yang, S. P. Shafi, L. Bi, Z. Wang, R. Peng, C. Xia, W. Liu, and Y. Lu, A high performance cathode for proton conducting solid oxide fuel cells, J. Mater. Chem. A **3**, 8405 (2015).
[22] W. Tan, D. Huan, W. Yang, N. Shi, W. Wang, R. Peng, X. Wu, and Y. Lu, A first-principles study on divergent reactions of using a $Sr_3Fe_2O_7$ cathode in both oxygen ion conducting and proton conducting solid oxide fuel cells, RSC Adv. **8**, 26448 (2018).
[23] K. Dong, J. Hou, L. Miao, Z. Jin, D. Wang, Y. Teng, and W. Liu, A comparative study of the R-P phase $Sr_{n+1}Fe_nO_{3n+1}$ (N = 1, 2 and 3) cathodes for intermediate temperature solid oxide fuel cells, Ceram. Int. **46**, 19335 (2020).
[24] Z. Jin, R. Peng, Y. Xia, Z. Wang, and W. Liu, Computational investigation of Zn-Doped and undoped $SrEu_2Fe_2O_7$ as potential mixed electron and proton conductors, RSC Adv. **10**, 39988 (2020).
[25] M. Lehtimäki, A. Hirasa, M. Matvejeff, H. Yamauchi, and M. Karppinen, Water-containing derivative phases of the $Sr_{n+1}Fe_nO_{3n+1}$ series, J. Solid State Chem. **180**, 3247 (2007).
[26] V. Øygarden, H. Fjellvåg, M. H. Sørby, and A. O. Sjåstad, Crystal structure of $LaSr_3Fe_3O_8(OH)_2 \cdot xH_2O$, Inorg. Chem. **55**, 7630 (2016).
[27] P. Adler, L. Schröder, K. Teske, M. Reehuis, A. Hoser, P. Merz, W. Schnelle, C. Felser, and M. Jansen, Oxygen deficiency in Sr_2FeO_{4-x}: Electrochemical control and impact on magnetic properties, Phys. Chem. Chem. Phys. **24**, 17028 (2022).
[28] M. Abbate, G. Zampieri, J. Okamoto, A. Fujimori, S. Kawasaki, and M. Takano, X-ray absorption of the negative charge-transfer material $SrFe_{1-x}Co_xO_3$, Phys. Rev. B **65**, 165120 (2002).
[29] M. Abbate, H. Ascolani, F. Prado, and A. Caneiro, Electronic structure and band gap of the negative charge-transfer material $Sr_3Fe_2O_7$, Solid State Commun. **129**, 113 (2004).
[30] Y. Ling, T. Guo, X. Zhang, R. A. Budiman, Y. Fujimaki, T. Nakamura, B. Lin, T. Kawada, and K. Amezawa, Evaluation of electrical conductivity and oxygen diffusivity of the typical Ruddlesden-Popper oxide $Sr_3Fe_2O_{7-\delta}$, Ceram. Int. **43**, 16264 (2017).
[31] S. E. Dann, M. T. Weller, and D. B. Currie, The synthesis and structure of Sr_2FeO_4, J. Solid State Chem. **92**, 237 (1991).
[32] D. Gryaznov, R. Merkle, E. A. Kotomin, and J. Maier, Ab initio modelling of oxygen vacancies and protonic defects in $La_{1-x}Sr_xFeO_{3-\delta}$ perovskite solid solutions, J. Mater. Chem. A **4**, 13093 (2016).
[33] Y. Ling, F. Wang, Y. Okamoto, T. Nakamura, and K. Amezawa, Oxygen nonstoichiometry and thermodynamic explanation of large oxygen-deficient Ruddlesden–Popper oxides $La_xSr_{3-x}Fe_2O_{7-\delta}$, J. Am. Ceram. Soc. **99**, 3792 (2016).
[34] E. V. Tsipis, E. N. Naumovich, M. V. Patrakeev, and V. V. Kharton, Oxygen intercalation in Ruddlesden-Popper type $Sr_3LaFe_3O_{10-\delta}$, Mater. Lett. **218**, 325 (2018).
[35] N. A. Szaro, S. C. Ammal, F. Chen, and A. Heyden, An ab initio study of the oxygen defect formation and oxide ion migration in $(Sr_{1-x}Pr_x)_2FeO_{4\pm\delta}$, J. Power Sources **515**, 230602 (2021).
[36] S. L. Dudarev, G. A. Botton, S. Y. Savrasov, C. J. Humphreys, and A. P. Sutton, Electron-energy-loss spectra and the structural stability of nickel oxide: An LSDA+U study, Phys. Rev. B **57**, 1505 (1998).
[37] G. Kresse and J. Furthmüller, Efficient iterative schemes for ab initio total-energy calculations using a plane-wave basis set, Phys. Rev. B **54**, 11169 (1996).
[38] M. F. Hoedl, A. Chesnokov, D. Gryaznov, R. Merkle, E. A. Kotomin, and J. Maier, Proton migration barriers in $BaFeO_{3-\delta}$–insights from DFT calculations, J. Mater. Chem. A **11**, 6336 (2023).
[39] See Supplemental Material at http://link.aps.org/supplemental/10.1103/v8m7-prgq for the detailed information on Sr_2FeO_4 and $SrFeO_3$ basic properties, Sr_2FeO_{4-d} defect configurations and their properties, the defect interaction and formation energies, the analysis of Fe oxidation state in Sr_2FeO_{4-d}, oxygen interstitial and vacancy migration in Sr_2FeO_{4-d}. The supplemental Material also contains Refs. [40,52,59].
[40] A. V. Krukau, O. A. Vydrov, A. F. Izmaylov, and G. E. Scuseria, Influence of the exchange screening parameter on the performance of screened hybrid functionals, J. Chem. Phys. **125**, 224106 (2006).
[41] P. E. Blöchl, Projector augmented-wave method, Phys. Rev. B **50**, 17953 (1994).
[42] D. Vanderbilt, Soft self-consistent pseudopotentials in a generalized eigenvalue formalism, Phys. Rev. B **41**, 7892 (1990).
[43] G. Kresse and D. Joubert, From ultrasoft pseudopotentials to the projector augmented-wave method, Phys. Rev. B **59**, 1758 (1999).
[44] H. J. Monkhorst and J. D. Pack, Special points for brillouin-zone integrations, Phys. Rev. B **13**, 5188 (1976).
[45] J. P. Perdew, K. Burke, and M. Ernzerhof, Generalized gradient approximation made simple, Phys. Rev. Lett. **77**, 3865 (1996).
[46] W. Tang, E. Sanville, and G. Henkelman, A grid-based bader analysis algorithm without lattice bias, J. Phys. Condens. Matter **21**, 84204 (2009).
[47] J. Speight, *Lange's Handbook of Chemistry*, Sixteenth Edition (McGraw-Hill Education LLC, New York, 2005).
[48] S. E. Dann, M. T. Weller, D. B. Currie, M. F. Thomas, and A. D. Al-Rawwas, Structure and magnetic properties of Sr_2FeO_4 and $Sr_3Fe_2O_7$ studied by powder neutron diffraction and Mössbauer spectroscopy, J. Mater. Chem. **3**, 1231 (1993).

[49] P. Adler, M. Reehuis, N. Stüsser, S. A. Medvedev, M. Nicklas, D. C. Peets, J. Bertinshaw, C. K. Christensen, M. Etter, A. Hoser, L. Schröder, P. Merz, W. Schnelle, A. Schulz, Q. Mu, D. Bessas, A. Chumakov, M. Jansen, and C. Felser, Spiral magnetism, spin flop, and pressure-induced ferromagnetism in the negative charge-transfer-gap insulator Sr_2FeO_4, Phys. Rev. B **105**, 054417 (2022).

[50] G. Zvejnieks, Y. Mastrikov, and D. Gryaznov, Jahn–teller distortion in Sr_2FeO_4: Group-theoretical analysis and hybrid DFT calculations, Sci. Rep. **13**, 16446 (2023).

[51] K. Momma and F. Izumi, VESTA: A three-dimensional visualization system for electronic and structural analysis, J. Appl. Crystallogr. **41**, 653 (2008).

[52] K. Okhotnikov, T. Charpentier, and S. Cadars, Supercell program: A combinatorial structure-generation approach for the local-level modeling of atomic substitutions and partial occupancies in crystals, J. Cheminform. **8**, 17 (2016).

[53] R. Grau-Crespo, A. Y. Al-Baitai, I. Saadoune, and N. H. De Leeuw, Vacancy ordering and electronic structure of γ-Fe_2O_3 (maghemite): A theoretical investigation, J. Phys. Condens. Matter **22**, 255401 (2010).

[54] M. Hoffmann, A. Ernst, W. Hergert, V. N. Antonov, W. A. Adeagbo, R. M. Geilhufe, and H. Ben Hamed, Magnetic and electronic properties of complex oxides from first-principles, Phys. Status Solidi **257**, 1900671 (2020).

[55] V. M. Zainullina, M. A. Korotin, and V. L. Kozhevnikov, Electronic structure of $SrFe_{1-x}(Mn, Co)_xO_{3-\delta}$: A CPA case study, J. Alloys Compd. **971**, 172660 (2024).

[56] J. Park, B. Xu, J. Pan, D. Zhang, S. Lany, X. Liu, J. Luo, and Y. Qi, Accurate prediction of oxygen vacancy concentration with disordered a-site cations in high-entropy perovskite oxides, npj Comput. Mater. **9**, 29 (2023).

[57] W. Xie, Y.-L. Lee, Y. Shao-Horn, and D. Morgan, Oxygen point defect chemistry in Ruddlesden-Popper oxides $(La_{1-x}Sr_x)_2MO_{4\pm\delta}$ (M = Co, Ni, Cu), J. Phys. Chem. Lett. **7**, 1939 (2016).

[58] V. I. Razumovskiy, Thermodynamics of vacancy formation in the CoCrFeMnNi high entropy alloy from DFT calculations, Asp. Min. Miner. Sci. **8**, 971 (2022).

[59] Y. A. Mastrikov, M. N. Sokolov, S. Koch, Y. F. Zhukovskii, A. Gopejenko, P. V. Vladimirov, V. A. Borodin, E. A. Kotomin, and A. Möslang, Ab Initio modelling of the initial stages of the ODS particle formation process, Nucl. Instruments Methods Phys. Res. Sect. B Beam Interact. with Mater. Atoms **435**, 70 (2018).

[60] SCRIPTS—Transition State Tools for VASP. https://theory.cm.utexas.edu/vtsttools/scripts.html (accessed 2024-03-10).

[61] G. Henkelman, B. P. Uberuaga, and H. Jónsson, A climbing image nudged elastic band method for finding saddle points and minimum energy paths, J. Chem. Phys. **113**, 9901 (2000).

[62] A. der Ven, G. Ceder, M. Asta, and P. D. Tepesch, First-principles theory of ionic diffusion with nondilute carriers, Phys. Rev. B **64**, 184307 (2001).

[63] J. H. Chang, P. B. Jørgensen, S. Loftager, A. Bhowmik, J. M. G. Lastra, and T. Vegge, On-the-fly assessment of diffusion barriers of disordered transition metal oxyfluorides using local descriptors, Electrochim. Acta **388**, 138551 (2021).

[64] A. J. Samin, D. A. Andersson, E. F. Holby, and B. P. Uberuaga, Ab initio based examination of the kinetics and thermodynamics of oxygen in Fe-Cr alloys, Phys. Rev. B **99**, 174202 (2019).

[65] X. Zhang, S. V. Divinski, and B. Grabowski, Ab Initio prediction of vacancy energetics in HCP Al-Hf-Sc-Ti-Zr high entropy alloys and the subsystems, Acta Mater. **227**, 117677 (2022).

[66] R. Dovesi, F. Pascale, B. Civalleri, K. Doll, N. M. Harrison, I. Bush, P. D'Arco, Y. Noël, M. Rérat, P. Carbonnière, M. Causà, S. Salustro, V. Lacivita, B. Kirtman, A. M. Ferrari, F. S. Gentile, J. Baima, M. Ferrero, R. Demichelis, and M. D. La Pierre, The CRYSTAL code, 1976–2020 and beyond, a long story, J. Chem. Phys. **152**, 204111 (2020).

[67] I. B. Bersuker, Four modifications of the jahn–teller effects. the problem of observables: Spin–orbit interaction, tunneling splitting, and orientational polarization of solids, Phys. Chem. Chem. Phys. **25**, 1556 (2023).

[68] I. B. Bersuker, Pseudo-Jahn–Teller effect—a two-state paradigm in formation, deformation, and transformation of molecular systems and solids, Chem. Rev. **113**, 1351 (2013).

[69] E. Niwa, K. Wakai, T. Hori, T. Nakamura, K. Yashiro, J. Mizusaki, and T. Hashimoto, Analysis of structural phase transition behavior of $Ln_2NiO_{4+\delta}$ (Ln: Nd, Pr) with variation of oxygen content, Solid State Ionics **262**, 724 (2014).

[70] T. Nakamura, K. Yashiro, K. Sato, and J. Mizusaki, Thermally-induced and chemically-induced structural changes in layered perovskite-type oxides $Nd_{2-x}Sr_xNiO_{4+\delta}$ (X = 0, 0.2, 0.4), Solid State Ionics **181**, 402 (2010).

[71] N. Hayashi, T. Yamamoto, A. Kitada, A. Matsuo, K. Kindo, J. Hester, H. Kageyama, and M. Takano, Field-induced ferromagnetism of Fe^{4+}-perovskite system, $Sr_{1-x}Ba_xFeO_3$ ($0 \leqslant x \leqslant 1$), J. Phys. Soc. Jpn. **82**, 113702 (2013).

[72] T. Das, J. D. Nicholas, and Y. Qi, Long-range charge transfer and oxygen vacancy interactions in strontium ferrite, J. Mater. Chem. A **5**, 4493 (2017).

[73] Y.-L. Lee, J. Kleis, J. Rossmeisl, Y. Shao-Horn, and D. Morgan, Prediction of solid oxide fuel cell cathode activity with first-principles descriptors, Energy Environ. Sci. **4**, 3966 (2011).

[74] M. F. Hoedl, Electronic structure and defect chemistry in iron perovskites, Ph.D. thesis University of Stuttgart, 2021.

[75] M. Vračar, A. Kuzmin, R. Merkle, J. Purans, E. A. Kotomin, J. Maier, and O. Mathon, Jahn-Teller distortion around Fe^{4+} in $Sr(Fe_xTi_{1-x})O_{3-\delta}$ from x-ray absorption spectroscopy, x-ray diffraction, and vibrational spectroscopy, Phys. Rev. B **76**, 174107 (2007).

[76] H. L. Lein, K. Wiik, and T. Grande, Thermal and chemical expansion of mixed conducting $La_{0.5}Sr_{0.5}Fe_{1-x}Co_xO_{3-\delta}$ materials, Solid State Ionics **177**, 1795 (2006).

[77] NIST Chemistry WebBook. https://webbook.nist.gov/chemistry/ (accessed 2024-06-05).

[78] D. Gryaznov, M. W. Finnis, R. A. Evarestov, and J. Maier, Oxygen vacancy formation energies in Sr-doped complex perovskites: Ab initio thermodynamic study, Solid State Ionics **254**, 11 (2014).

[79] A. Chesnokov, D. Gryaznov, and E. Kotomin, First principles calculations on CeO_2 doped with Tb^{3+} ions, Opt. Mater. (Amst). **90**, 76 (2019).

[80] J. Kilner and R. Brook, A study of oxygen ion conductivity in doped non-stoichiometric oxides, Solid State Ionics **6**, 237 (1982).

[81] A. E. Bocquet, A. Fujimori, T. Mizokawa, T. Saitoh, H. Namatame, S. Suga, N. Kimizuka, Y. Takeda, and M. Takano, Electronic structure of $SrFe^{4+}O_3$ and related Fe perovskite oxides, Phys. Rev. B **45**, 1561 (1992).

[82] S. Kitou, M. Gen, Y. Nakamura, K. Sugimoto, Y. Tokunaga, S. Ishiwata, and Taka-hisa Arima, Real-space observation of ligand hole state in cubic perovskite $SrFeO_3$, Adv. Sci. **10**, 2302839 (2023).

[83] Z. Li, R. Laskowski, T. Iitaka, and T. Tohyama, First-principles calculation of helical spin order in iron perovskite $SrFeO_3$ and $BaFeO_3$, Phys. Rev. B **85**, 134419 (2012).

[84] T. S. Bjørheim, M. F. Hoedl, R. Merkle, E. A. Kotomin, and J. Maier, Hydroxide ion, and oxide ion affinities of closed-shell oxides: Importance for the hydration reaction and correlation to electronic structure, J. Phys. Chem. C **124**, 1277 (2020).

[85] A. A. Sokol, A. Walsh, and C. R. A. Catlow, Oxygen interstitial structures in close-packed metal oxides, Chem. Phys. Lett. **492**, 44 (2010).

[86] R. A. Evarestov, A. Platonenko, D. Gryaznov, Y. F. Zhukovskii, and E. A. Kotomin, First-principles calculations of oxygen interstitials in corundum: A site symmetry approach, Phys. Chem. Chem. Phys. **19**, 25245 (2017).

[87] M. M. Kuklja, Y. A. Mastrikov, B. Jansang, and E. A. Kotomin, The intrinsic defects, disordering, and structural stability of $Ba_xSr_{1-x}Co_yFe_{1-y}O_{3-\delta}$ perovskite solid solutions, J. Phys. Chem. C **116**, 18605 (2012).

[88] T. Brudevoll, E. A. Kotomin, and N. E. Christensen, Interstitial-oxygen-atom diffusion in MgO, Phys. Rev. B **53**, 7731 (1996).

[89] A. Lushchik, V. N. Kuzovkov, E. A. Kotomin, G. Prieditis, V. Seeman, E. Shablonin, E. Vasil'chenko, and A. I. Popov, Evidence for the formation of two types of oxygen interstitials in neutron-irradiated $\alpha-Al_2O_3$ single crystals, Sci. Rep. **11**, 20909 (2021).

[90] Y. A. Mastrikov, R. Merkle, E. A. Kotomin, M. M. M. Kuklja, and J. Maier, Surface termination effects on the oxygen reduction reaction rate at fuel cell cathodes, J. Mater. Chem. A **6**, 11929 (2018).

[91] A. Kushima, D. Parfitt, A. Chroneos, B. Yildiz, J. A. Kilner, and R. W. Grimes, Interstitialcy diffusion of oxygen in tetragonal $La_2CoO_{4+\delta}$, Phys. Chem. Chem. Phys. **13**, 2242 (2011).

[92] A. Chroneos, D. Parfitt, J. A. Kilner, and R. W. Grimes, Anisotropic oxygen diffusion in tetragonal $La_2NiO_{4+\delta}$: Molecular dynamics calculations, J. Mater. Chem. **20**, 266 (2010).

[93] S. Xu, R. Jacobs, and D. Morgan, Factors controlling oxygen interstitial diffusion in the Ruddlesden–Popper oxide $La_{2-x}Sr_xNiO_{4+\delta}$, Chem. Mater. **30**, 7166 (2018).

[94] C. Tealdi, C. Ferrara, P. Mustarelli, and M. S. Islam, Vacancy and interstitial oxide ion migration in heavily doped $La_{2-x}Sr_xCoO_{4\pm\delta}$, J. Mater. Chem. **22**, 8969 (2012).

[95] E. J. Opila, H. L. Tuller, B. J. Wuensch, and J. Maier, Oxygen tracer diffusion in $La_{2-x}Sr_xCuO_{4-y}$ single crystals, J. Am. Ceram. Soc. **76**, 2363 (1993).

[96] D. Lee and H. N. Lee, Controlling oxygen mobility in Ruddlesden–Popper oxides, Materials (Basel). **10**, 368 (2017).